Chemical Engineering Journal 464 (2023) 142696

Contents lists available at ScienceDirect

Chemical Engineering Journal

journal homepage: www.elsevier.com/locate/cej

Plasma-enabled catalytic steam reforming of toluene as a biomass tar surrogate: Understanding the synergistic effect of plasma catalysis

Bin Xu [a], Jianjun Xie [a,*], Nantao Wang [b], Yanqin Huang [a], Huacai Liu [a], Xiuli Yin [a,*], Chuangzhi Wu [a], Xin Tu [b,*]

[a] CAS Key Laboratory of Renewable Energy, Guangdong Provincial Key Laboratory of New and Renewable Energy Research and Development, Guangzhou Institute of Energy Conversion, Chinese Academy of Sciences, Guangzhou 510640, China
[b] Department of Electrical Engineering and Electronics, University of Liverpool, Liverpool L69 3GJ, UK

ARTICLE INFO

Keywords:
Biomass gasification
Tar removal
Steam reforming of toluene
Plasma catalysis
Synergistic effect

ABSTRACT

In this study, steam reforming of toluene was carried out in a dielectric barrier discharge (DBD) plasma reactor combined with Ni/γ-Al_2O_3 catalysts. The effect of reaction temperature, calcination temperature of catalysts, and relative permittivity of packing materials, on the reaction performance and synergistic effect of plasma catalysis was investigated. The results showed that toluene conversion decreased initially and then increased with increasing temperature, due to a decreasing average reduced electric field and increasing catalytic activity at higher temperatures. At 450 °C, the process achieved a high toluene conversion of 87.1%, a total gas yield of 72.6%, and an energy efficiency of 18.2 g/kWh, demonstrating the potential of this approach for sustainable hydrogen production. Catalysts prepared at lower calcination temperatures or with higher relative permittivity packing materials perform better, owing to the larger Ni surface area available for catalytic reactions and the higher surface discharge facilitating the occurrence of surface reactions. In addition, the synergistic capacity in terms of toluene conversion and gas production exhibited a positive relationship with the metal surface area of catalysts and the relative permittivity of packing materials, while the relationship between reaction temperature and toluene conversion was negative.

1. Introduction

Recently, with the increasing depletion of fossil fuels and growing awareness of global warming, biomass has received increasing attention as an abundant and CO_2-neutral renewable energy source [1]. Gasification is one of the most promising technologies for converting biomass waste into fuel gases comprising H_2, CO, CH_4 and CO_2, given the high volatile matter content and low N, S and ash content of biomass feedstocks, as well as its operational simplicity and flexibility of use [2,3]. The fuel gas can be fed into gas engines or turbines to generate electricity and/or heat, or it can be further processed to produce hydrogen or syngas for fuel cells and Fischer-Tropsch synthesis, respectively [3]. However, during the gasification process, undesirable byproducts such as NH_3, NO_x, tar and fly ash are inevitably generated, with tar being one of the most troublesome contaminants [4]. Tar is typically a complex mixture of condensable hydrocarbons containing monocyclic to polycyclic aromatic hydrocarbons and oxygen-containing compounds that can condense on the available surface as operating temperatures fall below its dew point, resulting in clogging and corrosion problems [5,6]. Additionally, the tar content is highly influenced by the gasifier type and operating conditions, ranging from 0.5 to 100 g/m^3, which usually exceeds the permissible maximum of various downstream devices [7]. For example, the acceptable tar content of gasification fuel gas fed into internal combustion engines and gas turbines is typically below 100 mg/m^3 and 5 mg/m^3, respectively [8]. Therefore, efficient removal or conversion of tar is critical for the use of the gasification fuel gas.

Several methods for tar removal have been proposed, including mechanical separation, thermal cracking, and catalytic reforming. The use of mechanical separation could result in secondary environmental pollution and the loss of energy contained in tar [6]. In thermal cracking processes, high operating temperatures (>1000 °C) are typically required to achieve desirable performance, resulting in high energy consumption [9]. Although catalytic reforming can convert tar into valuable products at relatively low temperatures, its industrial application still faces two major challenges: firstly, high reaction temperatures (>600 °C) are still required, resulting in high energy costs; and

* Corresponding authors.
E-mail addresses: xiejj@ms.giec.ac.cn (J. Xie), xlyin@ms.giec.ac.cn (X. Yin), xin.tu@liverpool.ac.uk (X. Tu).

https://doi.org/10.1016/j.cej.2023.142696
Received 1 October 2022; Received in revised form 23 March 2023; Accepted 28 March 2023
Available online 30 March 2023

second, rapid deactivation of the catalysts due to sintering and carbon deposition compromises processing stability [10].

In addition to the aforementioned approaches, non-thermal plasma (NTP) technology is receiving increasing interest as a potential alternative for tar removal due to its ability to activate reactants under mild conditions [11,12]. In NTPs, the energetic electrons have a typical temperature of 1–10 eV, which is high enough to initiate chemical reactions, while keeping the gas temperature low [13]. Several types of NTP have been used for tar removal, including dielectric barrier discharge (DBD) [14–17], corona discharge [18,19], gliding arc discharge [20–22] and microwave discharge [23,24]. According to the literature, the advantages of using NTP for tar removal include high tar conversion, mild reaction conditions, and operational simplicity and convenience. However, the relatively high energy consumption and low selectivity toward the desired products may limit its industrial applications.

The introduction of heterogeneous catalysis into NTP, known as plasma catalysis, provides a promising approach to addressing the aforementioned issues through catalyst functionalities such as lowering activation energy and tuning product selectivity [25,26]. There are two configurations for the combination of NTP and solid catalysts: one-stage and two-stage. The one-stage configuration means that the catalyst is placed directly in the discharge zone, partially or completely filling the discharge gap, whereas the two-stage configuration means that the catalyst bed is typically placed next to the plasma reactor, with the one-stage configuration being the most common for plasma-catalytic tar removal [11]. Great efforts have been made to couple different types of NTP with catalysts for tar removal, such as corona discharge coupled with Ni/SiO_2 [27], DBD coupled with Ni/Al_2O_3 [28], Ni/ZSM-5 [29], Fe/Al_2O_3 [30], Mn@13X [17] and NiFe/(Mg, Al)O_x [31], and gliding arc discharge coupled with Ni/Al_2O_3 [20] and Ni-Co/Al_2O_3 [32], among others. When compared to the plasma-only system, the coupling process significantly improves tar conversion, selectivity and yield of target products and energy efficiency. Moreover, comparable performance can be achieved at low temperatures when compared to catalyst-only cases. Clearly, plasma catalysis is a promising alternative for achieving effective tar conversion under mild conditions.

The most attractive advantage of plasma catalysis is the potential to generate a synergistic effect by integrating NTP and catalyst, whereby the reaction performance achieved in the coupling system is better than the sum of those achieved in plasma-only and catalyst-only modes. Mei et al. combined gliding arc discharge and Ni-Co catalysts for steam reforming of mixed tar model compounds (toluene and naphthalene), and a synergistic effect was successfully obtained in terms of tar conversion, energy efficiency, and yield and selectivity for H_2, CO_2 and CH_4 [32]. In our previous study, toluene removal was carried out in a DBD reactor coupled with Ni catalysts using a simulating gasification gas. At 400 °C, the highest toluene removal of 91.7% was achieved, which was significantly higher than the sum (58.1%) of those obtained in the catalyst-only and plasma-only processes [33]. The synergistic effect is resulted from the complicated interactions between NTP and solid catalysts, and a detailed understanding of the synergistic effect is critical to facilitate the design and optimization of plasma reactors and catalysts, thus achieving better performance at a lower energy consumption. However, there has been very little research into the synergistic effect of plasma catalysis, particularly for tar removal. For instance, the relationship between the synergistic effect and key factors such as operating conditions and catalysts is unclear.

In this work, plasma-catalytic steam reforming of tar was carried out using a DBD reactor. Toluene was selected as a model tar compound as it is one of the main compounds with high thermal stability in tar products [34], and Ni/γ-Al_2O_3 was used as a catalyst because of its high activity and low cost. The effects of three key factors (reaction temperature, calcination temperature of catalysts and relative permittivity of packing materials) on reaction performance and synergistic effect were investigated. Moreover, the characteristics of both the discharge and the catalyst were investigated using various approaches to gain a better understanding of the synergistic effect in the plasma-catalytic reforming of tar.

2. Experimental

2.1. Catalyst preparation

The Ni/γ-Al_2O_3 catalysts used in this work were prepared using a wetness impregnation method. Before use, the commercial strip-shaped γ-Al_2O_3 support (diameter × length: 3 × (4 – 10) mm, specific surface area: 169 m^2/g, Jiangsu Jingjing New Materials Co., Ltd, China) was calcined in air at 550 °C for 3 h before being crushed and sieved to particle sizes of 40–60 mesh. An appropriate weight of γ-Al_2O_3 was added to an aqueous solution of $Ni(NO_3)_2{\cdot}6H_2O$ and impregnated overnight at room temperature. Following impregnation, the catalyst precursor was dried at 120 °C for 10 h and before being calcined in an air atmosphere for 4 h at different temperatures (450, 500, 550 and 600 °C). The as-prepared catalysts were labeled as NA(x), where x represents the calcination temperature. The accurate Ni loading was determined to be 8.9 wt% using the inductively coupled plasma optical emission spectroscopy (ICP-OES).

2.2. Catalyst characterization

The specific surface area and pore volume of the catalysts were determined by N_2 adsorption/desorption isotherms at −196 °C using a surface area analyzer (ASAP 2010, Micromeritics). Prior to the measurement, the samples were degassed at 200 °C for 10 h under vacuum.

Powder X-ray diffraction (XRD) measurements were performed on an X-ray diffractometer (PANalytical, X'pert Pro MPD) equipped with a Cu Kα ($\lambda = 0.154$ nm) radiation source (40 kV and 40 mA) in the scanning range of 10-80°. The average crystallite size of Ni nanoparticles (NPs) was calculated by Scherer's equation [35]:

$$D_{Ni} = K \times \lambda/(\beta \times \cos\theta) \quad (1)$$

where the dimensionless shape factor K is 0.9, and β is the full width at half maximum of the Ni (200) peak at 51.7°.

H_2-temperature programmed reduction (H_2-TPR) measurements were carried out on a TPR instrument (ChemStar, Quantachrome). Before the measurement, 50 mg of sample was preheated in a He stream at 300 °C for 30 min before being cooled to room temperature. The reaction chamber was then filled with 50 mL/min of 10 vol% H_2/Ar gas while the temperature was raised from 40 to 900 °C at a heating rate of 10 °C/min.

The CO_2 and NH_3 temperature programmed desorption (CO_2-TPD and NH_3-TPD) were performed on a TPD instrument (ChemStar, Quantachrome). Prior to the adsorption, 150 mg of sample was reduced at 650 °C in 10 vol% H_2/Ar (50 mL/min) for 1 h and then cooled to 50 °C in He flow. The sample was subsequently heated to 50 °C or 100 °C for CO_2 or NH_3 adsorption, respectively. The adsorption of CO_2 or NH_3 was conducted by flowing pure CO_2 or 7.9 vol% NH_3/He (50 mL/min) through the sample, respectively. After adsorption for 1 h, the sample was purged with the He flow until baseline stabilization, and then heated up to 800 °C with a heating rate of 10 °C/min in the He flow (50 mL/min). The corresponding TPD spectra were obtained by monitoring the desorbed CO_2 or NH_3 using a thermal conductivity detector.

The pulse chemisorption of CO was carried out on a chemisorption apparatus (AutoChem II 2920, Micromeritics). Prior to the measurement, 0.5 g of sample was reduced at 650 °C for 1 h in a 10 vol% H_2/Ar (50 mL/min) atmosphere and then cooled to 50 °C in He flow. The CO chemisorption was operated by injecting 0.5 mL of 8 vol% CO/He and repeating the procedure every 6 min until the CO peaks became identical. The CO uptake was measured by a thermal conductivity detector and used for the calculation of the Ni metal surface area using the

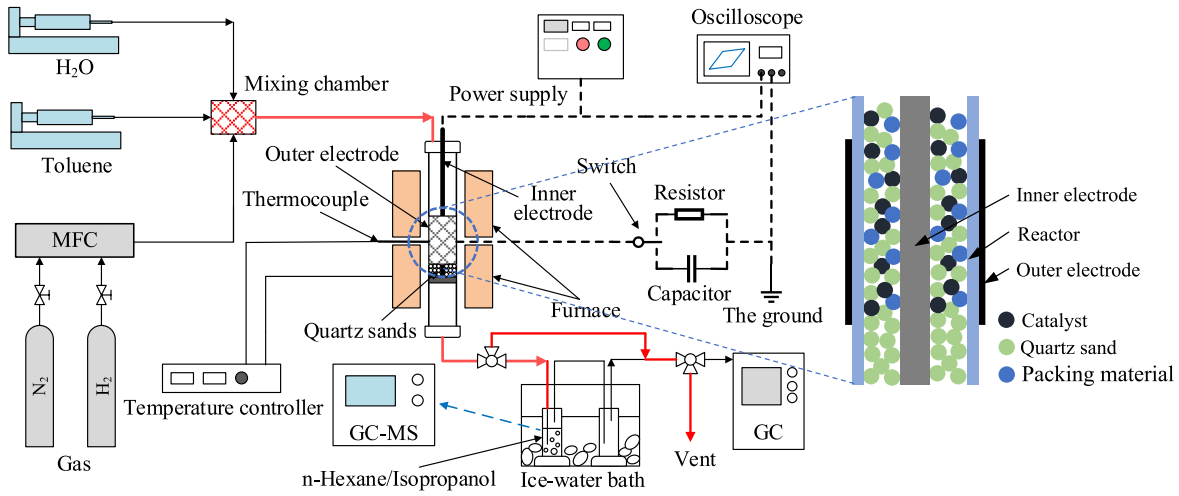

Fig. 1. Schematic diagram of the experimental setup.

following equation [36]:

$$SA_{Ni}\left(\mathrm{m^2/g\text{-}catal.}\right) = \mathrm{X} \times \mathrm{SF} \times \mathrm{N} \times \mathrm{RA} \quad (2)$$

where X is the CO uptake in moles per gram of catalyst (mol/g-catal.), SF is the stoichiometric factor (1), N = 6.023×10^{23} Ni atoms/mol, and RA is the atomic cross-sectional area of Ni (0.0649 nm^2).

In addition, the dispersion degree (%*D*) and the average particle size (d_{Ni}) of Ni were calculated by the following equations [37]:

$$\%D = 1.17 \times \mathrm{X}/(W \times f) \quad (3)$$

$$d_{Ni}(\mathrm{nm}) = 97.1/\%D \quad (4)$$

where *W* is the weight percentage of nickel, and *f* is the reduction degree.

Thermogravimetric analysis (TG, STA409PC, NETZSCH) combined with a mass spectrometry (MS, QMS403, NETZSCH) was used to characterize the spent catalysts. The samples were heated from 40 °C to 900 °C at a heating rate of 10 °C/min and an air flow rate of 30 mL/min.

The FTIR spectra of spent catalysts were recorded by an infrared spectrometer (INVENIO-S, Bruker) in the range of 400–4000 cm^{-1} with a resolution of 4 cm^{-1}. Before the measurement, 1 mg of each sample was mixed with 100 mg of KBr (purity > 99%, Aladdin), and the mixtures were pressed into wafers with a diameter of 13 mm.

Catalyst surface analysis was performed on an XPS instrument (ESCALAB 250Xi, Thermo Fisher) equipped with an Al (Kα) (hv = 1486.6 eV) X-ray radiation source. All binding energies were calibrated based on the C1s hydrocarbon peak at 284.6 eV.

2.3. Experimental setup

Fig. 1 shows a schematic diagram of the experimental setup. The DBD reactor consists of a cylindrical corundum ceramic tube (i.d. 19 mm, o.d. 25 mm) wrapped with a 50-mm-long stainless-steel mesh as the outer electrode. A stainless-steel rod (diameter 16 mm) is placed along the axis of the tube as the inner electrode. Hence, the discharge gap is 1.5 mm with a corresponding discharge volume of ~4.1 mL. The catalysts were held in place by a stainless-steel sieve attached to the end of the inner electrode, and quartz sand (40–60 mesh) was used to fill the region between the lower edge of the discharge zone and the stainless-steel sieve. In the experiments, 0.4 g of catalyst (about 0.8 mL), 1 mL of packing material (quartz, corundum, zirconia ceramics or silicon carbide) and 3 mL of quartz sand, all having the same particle size of 40–60 mesh, were placed at the discharge zone after being fully mixed. Then, plasma catalysis and catalyst-only modes can be achieved by turning the plasma on and off, respectively. In addition, the catalyst can be replaced by quartz sand with the same particle size to evaluate the performance of a plasma-only mode. The DBD reactor was placed inside a tubular furnace with a temperature range of room temperature to 750 °C. The reaction temperature was measured using a K-type thermocouple located on the outside reactor tube wall at the midpoint of the discharge zone after the reaction reached a stable stage. The catalysts were reduced in situ in a flowing 10 vol% H_2/N_2 at 650 °C for 1 h before the experiments. After each experiment, the reactor was cleaned by heating it to 700 °C for 1 h in an air atmosphere to remove carbon deposition and other contaminants formed during the reactions.

Toluene and H_2O were pumped into the mixing chamber by two syringe pumps (LSP01-1A, Longer Pump) with a flow rate of 5.196 μL/min and 11.64 μL/min, respectively, to attain a constant steam/carbon (S/C) molar ratio of 2. Subsequently, toluene and H_2O were vaporized and mixed with 133 mL/min carrier gas (N_2) in a mixing chamber with a temperature of 250 °C before being fed into the DBD reactor. The produced gas stream passed through two absorption bottles, which were connected in-line and placed in an ice water bath. The former one contained 50 mL of n-hexane or isopropanol solvent to collect unconverted toluene or condensable byproducts, respectively, while the latter was left empty to collect entrained droplets. To avoid condensation of water vapor, toluene and liquid products, the pipeline between the mixing chamber and the inlet, as well as the pipeline connecting the outlet to the absorption bottle and the vent were heated to 200 °C during the experiments.

The plasma was generated by an AC high voltage power supply (CTP-2000 K, Nanjing Suman) with a peak voltage of 30 kV and a frequency of 5–20 kHz. The frequency was kept at 7.5 kHz in this work. The applied voltage (V) of the DBD reactor was measured by a high voltage probe (P6015A, Tektronix). The charge (Q) and current were obtained by measuring the voltage drops on a capacitor (0.1 μF) and a resistor (200 Ω), respectively. These signals were recorded by a digital oscilloscope (DPO2024B, Tektronix). In this work, the discharge power was determined by multiplying the area of the V-Q Lissajous diagram with the frequency and was fixed at 13 ± 0.5 W.

2.4. Methods of analysis

The unconverted toluene and by-product (benzene) collected by the n-hexane-containing bottle in 5 min were analyzed using gas chromatography (GC, GC-2014, Shimadzu) equipped with a capillary column (AE-PEG-20 M, ATEO) and a flame ionization detector. The gas products were analyzed by an online gas chromatography system (GC, Micro GC490, Agilent) equipped with two thermal conductivity detectors, as

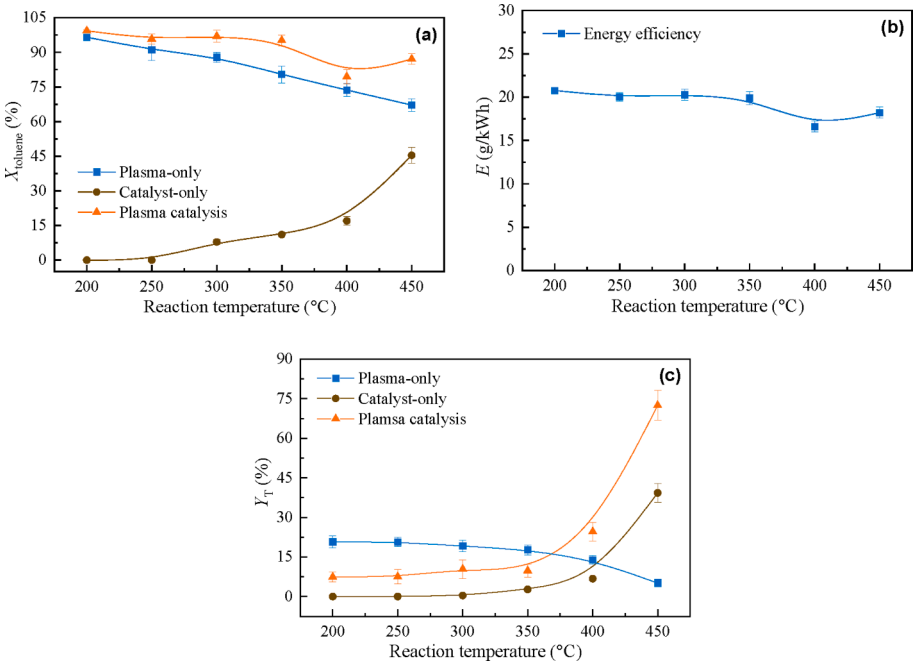

Fig. 2. Effect of reaction temperature on toluene conversion (a), total gas yield (b) and energy efficiency (c) (Catalyst: NA(500); Packing material: quartz).

well as a Molsieve 5A and PoraPLOT Q column. After a 1 h reaction, liquid products were collected by the isopropanol-containing bottle and analyzed by an off-line gas chromatography-mass spectrometry instrument (GC–MS, Thermo Fisher, Trace 1300-ISQ) equipped with a DB-5 ms column (Agilent). Further details on the GC and GC–MS measurements are presented in Table S1.

The toluene conversion $X_{toluene}$ and energy efficiency E were determined by following equation:

$$X_{toluene}\ (\%) = \frac{[T]_{in} - [T]_{out}}{[T]_{in}} \times 100 \quad (5)$$

$$E\ (g/kWh) = \frac{[m]_{removal}}{P \times 60/3600000} \quad (6)$$

where $[T]_{in}$ and $[T]_{out}$ represent the molar concentration of toluene at the inlet and outlet, respectively, and P represents the discharge power in watt and $[m]_{removal}$ represents the grams of toluene removed per minute.

Note that the external heat power was not taken into account in the calculation of energy efficiency, in consistence with previous works [29,30,38].

The yield Y and selectivity S of the products, and the total gas yield Y_T were calculated by equations 7–12. As we cannot measure the conversion of H_2O in this study, the selectivity of H_2 cannot be determined.

$$Y_{H_2}\ (\%) = \frac{[H_2]_{out}}{4 \times [T]_{in} + [H_2O]_{in}} \times 100 \quad (7)$$

$$Y_{CO_x}\ (\%) = \frac{[CO_x]_{out}}{7 \times [T]_{in}} \times 100 \quad (8)$$

$$Y_{C_xH_y}\ (\%) = \frac{x \times [C_xH_y]_{out}}{7 \times [T]_{in}} \times 100 \quad (9)$$

$$S_{CO_x}\ (\%) = \frac{[CO_x]_{out}}{7 \times ([T]_{in} - [T]_{out})} \times 100 \quad (10)$$

$$S_{C_xH_y}\ (\%) = \frac{x \times [C_xH_y]_{out}}{7 \times ([T]_{in} - [T]_{out})} \times 100 \quad (11)$$

$$Y_T\ (\%) = \frac{[H_2]_{out} + [CO]_{out} + [CO_2]_{out} + [CH_4]_{out} + [C_2]_{out} + [C_3]_{out}}{[T]_{in} + [H_2O]_{in}} \times 100 \quad (12)$$

where $[H_2]_{out}$, $[CO_x]_{out}$, $[C_xH_y]_{out}$ are the molar amounts of H_2, CO_x (CO and CO_2) and C_xH_y (CH_4, C_2H_2, C_2H_4, C_2H_6, C_3H_6, C_3H_8 and C_6H_6) at the outlet, respectively, and $[H_2O]_{in}$ is the molar amount of H_2O at the inlet. C_2 contains C_2H_2, C_2H_4 and C_2H_6, and C_3 includes C_3H_6 and C_3H_8.

The carbon balance B_C of the plasma catalytic process was determined by equation (13).

$$B_C\ (\%) = \sum S_{C_xH_y}\ (x = 1, 2, 3, 6)\ (\%) + S_{CO_x}\ (x = 1, 2)\ (\%) \quad (13)$$

The synergistic capacity SC was used to evaluate the intensity of the synergistic effect between plasma and catalysts and calculated by equation (14).

$$SC_{\xi}(\%) = \frac{\xi_{p+c} - \xi_p - \xi_c}{\xi_p + \xi_c} \times 100 \quad (14)$$

Where ξ can be the toluene conversion, and the yield and selectivity of gas products. The subscripts, p + c, p and c, represent the performances obtained by plasma catalysis, plasma-only and catalyst-only, respectively.

3. Results and discussion

3.1. Effect of reaction temperature

3.1.1. Reaction performance

Fig. 2a shows the toluene conversion obtained in the plasma-only, catalyst-only and plasma catalysis modes at different reaction temperatures. Quite different removal behaviors are observed among these processes. In the catalyst-only system, the conversion of toluene increased progressively with increasing reaction temperature, reaching a maximum of 45.4% at 450 °C. However, in the plasma-only system, the toluene conversion gradually decreased from 96.5% at 200 °C to 67.1%

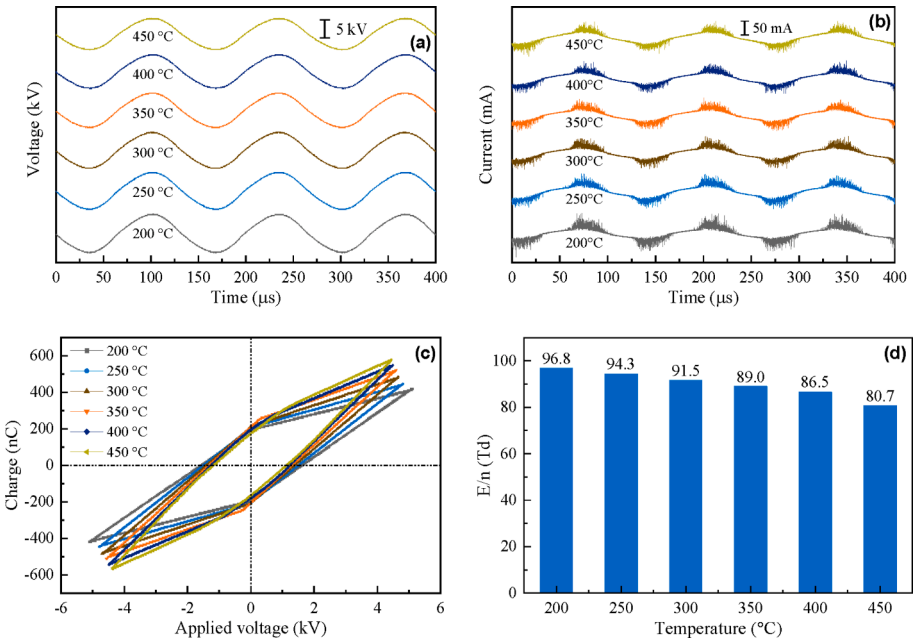

Fig. 3. Electrical signals of the DBD at different reaction temperatures: Applied voltage signals (a), current signals (b), V-Q Lissajous curves (c) and E/n (d) (Catalyst: NA(500); Packing material: quartz).

at 450 °C. In the plasma catalysis process, the conversion of toluene reached a maximum of ~100% at 200 °C, then remained at ~95% in the temperature range of 250 °C to 350 °C, then declined to 79.4% at 400 °C, followed by a rise to 87.1% at 450 °C. Consistent with the change trend of the conversion, the energy efficiency of plasma catalysis first decreased and then increased with increasing temperature, ranging from 16.6 to 20.8 g/kWh (Fig. 2b). Fig. 2c shows the effects of reaction temperature on total gas yield. In contrast to the decreasing trend observed in the plasma-only mode, an increase in total gas yield with temperature is observed in both catalyst-only and plasma catalysis modes, especially above 350 °C, indicating that the efficient production of gas products is strongly dependent on catalysts. At 450 °C, the maximum gas yields for catalyst-only and plasma catalysis were 39.2% and 72.6%, respectively. As a result, the combination of NTP and catalysts at 450 °C achieved 87.1% toluene conversion, 72.6% total gas yield and 18.2 g/kWh energy efficiency, outperforming the plasma-only and catalyst-only modes.

The effect of reaction temperature on the selectivity and yield of gas products and benzene is presented in Figs. S1, S2 and S3. In the plasma-only system, the selectivity and yield of gas products and benzene maintain below 14% within the temperature range of 200–400 °C, with CO and H_2 being the main products. When the temperature increased to 450 °C, the selectivity and yield of CO, H_2, and C_2 dropped significantly to 2%, becomes the dominating component in produced gases. In the catalyst-only case, due to the increasing catalytic activity, at higher temperatures all gas products obtain higher selectivity and yield values, which are much higher than those in the plasma-only mode. H_2, CO, CO_2 and benzene were the major products, and particularly, the selectivity of benzene was even up to 45%, which is an unsatisfactory result considering the steam reforming pursuing the production of combustible gases. In plasma catalysis, the selectivity and yield of CO, CO_2 and H_2, at temperatures below 350 °C, maintain less than 10%, and then increase markedly with rising temperature, obtaining the maximums, most of which are higher than those obtained by catalyst-only. Meanwhile, the plasma catalytic process greatly lowers the selectivity of benzene, CO, H_2 and CO_2 being the main products. For instance, at 450 °C, the CO selectivity is up to nearly 50% with a corresponding yield of about 45%, together with the selectivity of benzene of less than 10%.

At temperatures below 350 °C, plasma catalysis shows satisfactory results in converting toluene (Fig. 2), but its poor performance in generating gas products indicates that most of the toluene is converted into liquid products and/or carbon deposition. This carbon deposition is an unwanted byproduct that can reduce the catalytic activity by blocking active sites and lowering the discharge power, leading to a decline in plasma catalysis performance [28]. To gain a better understanding of reaction products, liquid products and carbon deposition produced at temperatures of 200 °C and 450 °C were analyzed. Researchers conducted GC–MS analysis of liquid products and TG-MS, FTIR, and XPS analysis of spent catalysts, and the results are shown in Fig. S5, Table S2, and Fig. S6. At 200 °C, most of the toluene was converted into carbon deposition, which was mainly composed of aliphatic carbon and easier to eliminate. At 450 °C, the increasing catalytic activity improved the oxidation reactions of carbonaceous species, leading to a decrease in the amount of carbon deposits and a corresponding increase in CO and CO_2 production. Additionally, at both temperatures, a small portion of the removed toluene was converted into liquid products with a molecular weight greater than benzene. The number and relative area of O- and N-containing compounds were higher at 200 °C than at 450 °C. These liquid products were formed through reactions between intermediates and fragments or radicals, such as CN and OH radicals [39].

Previous studies have shown that changes in reaction temperature can affect the physical properties of plasma and influence its chemistry [40,41]. Thus, we investigated the discharge characteristics of the DBD at different temperatures. The packed-bed effect in this study resulted in a combination of filamentary discharge and surface discharge. The introduction of packing material pellets reduced the available discharge volume, leading to the formation of filaments only in the void between the pellets and the reactor wall. Furthermore, an increased electric field, due to polarization effects and charge accumulation, was found to be mainly located around the contact points between the pellets, where surface discharge was formed and propagated along the surface [42,43]. Fig. 3 shows the electrical signals of the DBD operating at different temperatures with a fixed discharge power. The current signal of the discharge was quasi-sinusoidal with multiple superimposed current pulses per half-cycle of the applied voltage. When the reaction temperature increased from 200 °C to 450 °C at the same discharge power, the magnitude of the current pulses decreased, but the displacement

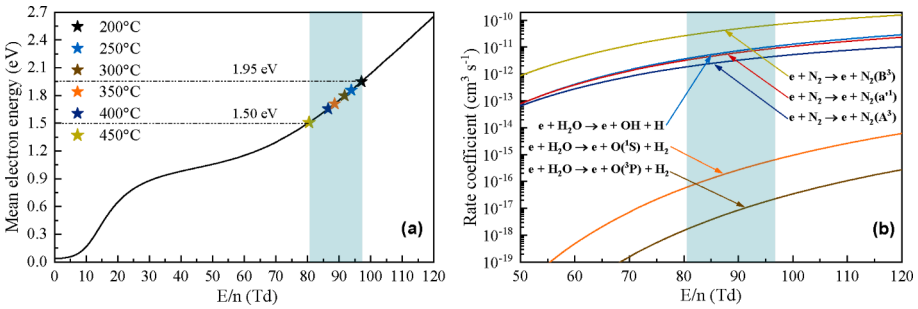

Fig. 4. Calculated mean electron energy (a) and rate coefficients of electron impact reactions (b) at different E/n (Catalyst: NA(500); Packing material: quartz).

current increased correspondingly, as well as the applied voltage decreasing from 10.4 kV_{pk-pk} to 8.8 kV_{pk-pk} (as shown in Fig. 3a and b). These changes indicate that filamentary discharge weakened while the component of surface discharge increased at high temperatures [42,44].

Fig. 3c shows the Lissajous curves of the DBD at different reaction temperatures while keeping the discharge power constant. As the temperature increases, the shape of the curve transforms from a parallelogram to an oval, indicating changes in the discharge characteristics. The Lissajous curve enables us to determine the the onset voltage (U_{on}) and the effective capacitances of the dielectric barrier (C_d) and the total system (C_{tot}). Using these parameters, we can calculate the capacitance of the gas (C_g), the breakdown voltage in the gas gap (U_b), and the average reduced electric field (E/n). The calculation process is detailed in section 6 of the Supporting Information. Table S3 summarizes the estimated parameters at different temperatures. Fig. 3d shows the E/n decreases from 96.8 Td to 80.7 Td as the temperature increases from 200 °C to 450 °C. This phenomenon has also been observed in plasma-assisted cellulose reforming [40] and plasma CH_4 reforming [41].

Furthermore, the mean electron energy at different E/n values can be calculated using the Boltzmann equation and BOLSIG+ [45–47], as shown in Fig. 4a. The mean electron energy increases with rising E/n, however, as temperature increases in the range of 200–450 °C, it progressively declines from 1.95 eV to 1.50 eV. This decline in mean electron energy weakens the plasma chemistry trigger, which negatively impacts the reaction performance of plasma. In the plasma toluene steam reforming process, important active species such as excited N_2 molecules, OH and O radicals initiate and drive reactions [38,48]. Hence, the rate coefficients of the electron impact reactions leading to the formation of these species were calculated using BOLSIG+, and are shown in Fig. 4b. The rate coefficient of all reactions increases with increasing E/n, implying that higher rate coefficients can be achieved at lower temperatures. This result suggests that higher reaction temperatures are not favorable for generating excited species and radicals that can effectively decompose toluene.

The analysis presented above allows us to draw several conclusions regarding reaction performance. In plasma catalysis, the destruction of toluene depends heavily on plasma intensity at low temperatures. The decreasing E/n caused by rising temperatures lowers the mean electron energy, reducing the production of active species, and subsequently leading to a decrease in conversion. The higher E/n values are more favorable for ring cleavage of aromatic intermediates and toluene, which is mainly initiated through reactions with energetic electrons and excited N_2 [49,50]. This could explain the higher aliphatic nature of the carbon deposits formed at low temperatures. At high temperatures, the increased catalytic activity plays a crucial role in toluene destruction, reversing the declining trend in conversion. Furthermore, the efficient formation of gaseous products is strongly dependent on catalysis, and a significant increase in gas production can only be observed at high temperatures where catalytic activity has notably increased, accompanied by a correspondingly significant decrease in carbon deposits.

3.1.2. *Synergistic effect*

The synergistic effect of the process was evaluated by analyzing the toluene conversion and total gas yield. Fig. 5a displays the values of synergistic capacities at different reaction temperatures. Synergistic capacities were calculated to evaluate the synergistic effect for toluene conversion and gas production. The results showed that the synergistic effect can only be achieved at temperatures below 350 °C for toluene conversion with a capacity of about 4%. However, the synergistic capacity decreases with increasing temperature from 350 to 450 °C. On the other hand, for gas production, the synergistic capacities remained negative at around −50%, at temperatures between 200 and 350 °C. The synergistic effect increased with temperature, reaching about 65% at 450 °C. Fig. S8 presents the synergistic capacities calculated using selectivity and yield of gas products. No synergistic effect was observed in terms of both selectivity and yield of all gas products at temperatures lower than 350 °C. At higher temperatures, the synergistic effect was concentrated in the yield of the main gas products (H_2, CO and CO_2), and the synergistic capacity significantly increased with temperature.

The relationship between reaction temperature and the synergistic capacity in terms of toluene conversion and gas production is shown in Fig. 5b. The temperature dependence curve can be divided into two parts based on a threshold temperature of 350 °C. Below 350 °C, although the linear fitting method cannot achieve a satisfactory result,

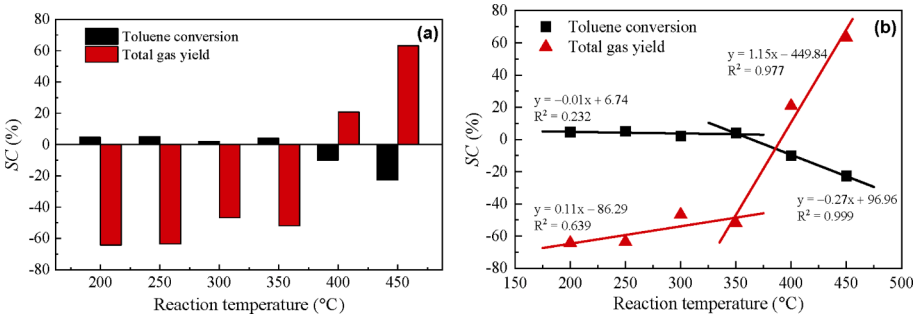

Fig. 5. Effect of reaction temperature on the synergistic capacity calculated using toluene conversion and total gas yield (a), and correlation between the reaction temperature and the synergistic capacity (b) (Catalyst: NA(500); Packing material: quartz).

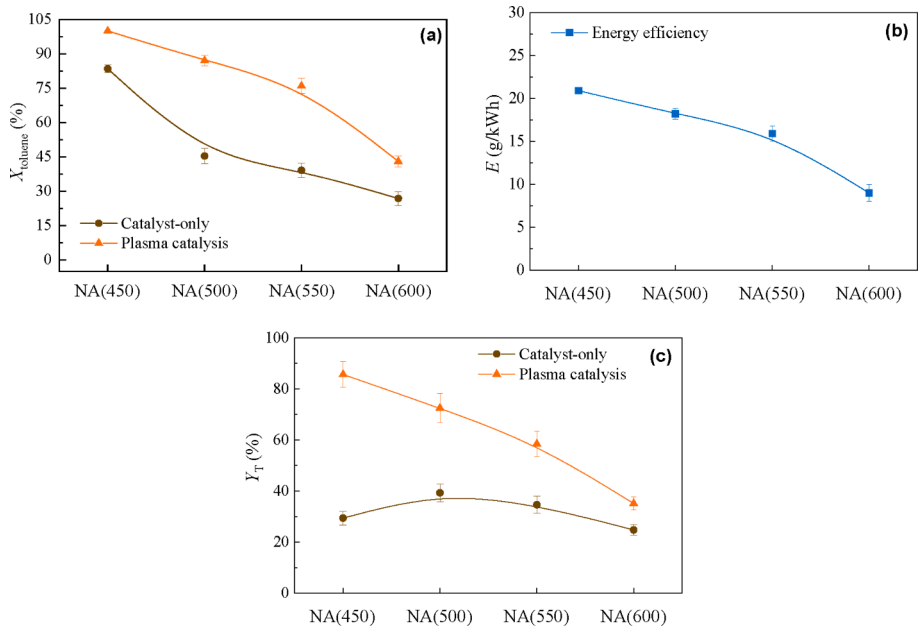

Fig. 6. Effect of calcination temperature of catalysts on toluene conversion (a), total gas yield (b) and energy efficiency (c) (Reaction temperature: 450 °C; Packing material: quartz).

the low slope of the fitted straight line suggests a weak temperature dependence of the synergistic capacity in this temperature range. Above 350 °C, however, the relationship between temperature and synergistic capacity is linear and significant. The synergistic capacity in toluene conversion and gas production shows negative and positive temperature dependence, respectively.

The catalytic performance of the catalyst and discharge characteristics of the DBD suggest that increasing the temperature from 200 °C to 450 °C enhances the formation of surface discharge and decreases the E/n. By contrast, the activity of the catalyst increases significantly above a threshold temperature of 350 °C (Figs. 2 and S2). The threshold temperature for the rapid increase in catalytic activity is consistent with the threshold temperature for the change in synergistic capacity. This suggests that the variation in catalytic activity plays a more important role in the generation of the synergistic effect compared to the discharge characteristics.

In summary, the synergistic effect of plasma catalysis in the steam reforming of toluene is largely determined by the catalytic activity of the catalyst and is therefore greatly influenced by the reaction temperature. The synergistic effect is most pronounced at temperatures above 350 °C and is particularly noticeable in terms of gas production. Above this threshold temperature, there is a strong linear relationship between the synergistic capacity and the reaction temperature, with a negative correlation in toluene conversion and a positive correlation in gas production.

3.2. Effect of calcination temperature of catalysts

3.2.1. Reaction performance

The effect of calcination temperature on the performance of catalysts and the synergistic effect in steam reforming of toluene is discussed in this section. The experiments were conducted at 450 °C, which is the most suitable operating temperature for the plasma-catalytic process in this study. It is worth mentioning that the results obtained in the plasma-only mode in this section are equivalent to the results obtained at 450 °C in the previous section. This was achieved by replacing the catalyst with quartz sands to create a plasma-only mode in the study. Fig. 6a shows the effect of different calcination temperatures on toluene conversion. It can be seen that an increase in calcination temperature leads to a decrease in both the catalyst-only and plasma-catalytic modes of conversion. For example, when the packing material is changed from NA (450) to NA(600), the conversion in the catalyst-only mode drops from 84% to 27% and in plasma catalysis it decreases from 100% to 43%. This is accompanied by a significant decrease in energy efficiency, from 20.9 g/kWh to 9.0 g/kWh (Fig. 6b). The 100% toluene conversion and 20.9 g/kWh energy efficiency achieved with NA(450) as a catalyst is a competitive result, especially in DBD systems, compared to similar works listed in Table S5. The total gas yield is presented in Fig. 6c. In the catalyst-only mode, the yield ranges from 25% to 40% and NA(500) and NA(600) give the maximum and minimum, respectively. In plasma catalysis, the total gas yield decreases significantly with the increase in the calcination temperature of the catalyst, from 85% with NA(450) packing to 35% with NA(600) packing. The results suggest that the use of a catalyst with a low calcination temperature is favorable for both toluene conversion and gas production in plasma catalysis.

Table 1
Specific area, pore volume and mean pore size of the catalysts.

Catalysts	BET surface area (m^2/g)	Pore volume (cm^3/g)	Mean pore size (nm)
γ-Al_2O_3	169.2	0.48	11.3
NA(450)	141.0	0.41	11.5
NA(500)	139.4	0.40	11.5
NA(550)	135.0	0.40	11.8
NA(600)	134.8	0.40	11.9

The results show that the selectivity and yield of gas products and benzene are influenced by the calcination temperature of the catalysts used (Figs. S11 and S12). As the calcination temperature of the catalysts increases, the selectivity of CO and benzene increases (Fig. S11), while the selectivity of CO_2 achieves the highest value with NA(500). The yield of CO, CO_2 and H_2 decreases with the increasing calcination temperature of the catalysts used. The selectivity and yield of CH_4, C_2, and C_3 is less than 2% and is not significantly influenced by the change of catalysts packed. In plasma catalysis, the selectivity of CO is kept at 50–60% and the benzene selectivity is significantly reduced compared to the catalyst-only process. The yield of the main gas products decreases with increasing calcination temperature of the catalysts.

Apparently, the calcination temperature of catalysts strongly

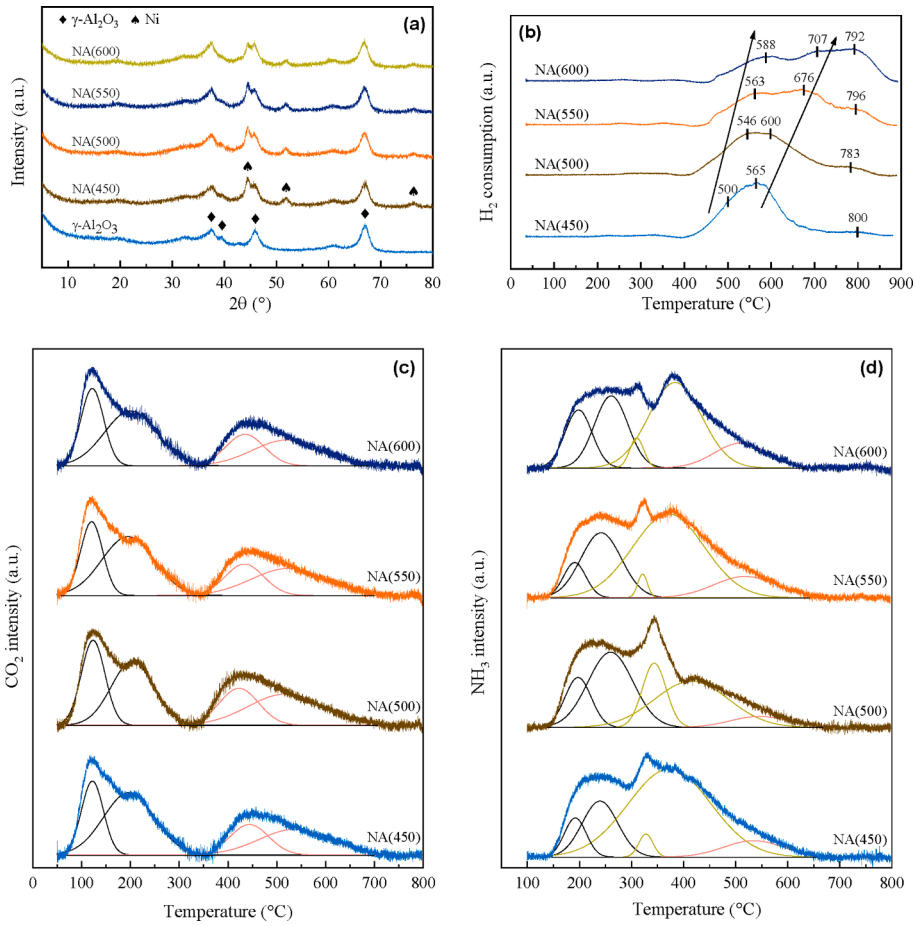

Fig. 7. XRD patterns (a), H_2-TPR profiles (b), CO_2-TPD (c) and NH_3-TPD (d) profiles of the catalysts.

Table 2
Basic and acidic site distribution of the catalysts.

Catalysts	Base site distribution and density			Acid site distribution and density			
	L (%)	H (%)	Total (μmol/g)	L (%)	M (%)	H (%)	Total (μmol/g)
NA(450)	61.2	38.8	131.3	24.9	66.5	8.6	460.9
NA(500)	55.6	44.4	133.4	45.6	48.2	6.2	403.5
NA(550)	59.4	40.6	134.2	31.1	56.8	12.1	416.5
NA(600)	60.7	39.1	129.6	38.8	48.3	12.9	401.8

Note: L (50–350 °C) and H (350–700 °C) represent the low- and high-temperature peak respectively in CO_2-TPD; L (100–300 °C), M (300–450 °C) and H (450–700 °C) represent the low-, medium- and high-temperature peak respectively in NH_3-TPD.

Table 3
CO pulse chemisorption result of the catalysts.

Catalysts	Reduction degree (%)[a]	CO uptake (μmol/g)	Ni surface area (m^2/g-catal.)	Dispersion (%)	Ni particle size (nm)
NA(450)	87.8	31.1	1.22	2.34	27.7
NA(500)	78.2	26.6	1.04	2.24	28.9
NA(550)	50.7	22.1	0.86	2.87	22.5
NA(600)	30.2	14.0	0.55	3.06	21.1

[a] Reduction degree was estimated using the ratio of the peak area below 650 °C with respect to the total peak area in H_2-TPR profile.

influences the reaction performance of plasma catalysis in terms of removal capacity and gas production. To better understand this effect, various characterization techniques, such as BET, XRD, H_2-TPR, CO_2–/NH_3-TPD and CO pulse chemisorption, were employed. As shown in Table 1, with increasing calcination temperature from 450 °C to 600 °C, the surface area of the catalyst decreases slightly from 141.0 m^2/g to 134.8 m^2/g, while the mean pore size rises from 11.5 nm to 11.9 nm. The XRD patterns of the reduced catalysts are presented in Fig. 7a. The main peaks at 44.3°, 51.6° and 76.3° correspond to metallic nickel, and the calculated nickel particle sizes (6.1 and 6.8 nm) are slightly influenced by the calcination temperature. Fig. 7b shows the H_2-TPR profiles of the catalysts calcined at different temperatures. The three main peaks, the low-, medium- and high-temperature peak, correspond to free NiO species, the NiO specie with stronger interactions with the support, and stable nickel aluminate with a spinel structure, respectively [51]. The increase of calcination temperature results in a shift of the low- and medium-temperature peaks to higher temperatures, as well as an increase in the intensity of the high-temperature peak. It indicates that a high calcination temperature strengthens the interaction between NiO species and the support, which is unfavorable for the reduction of NiO species during the activation treatment and leads to a decreased reduction degree of the catalysts. The basic and acidic properties of the catalysts were characterized by CO_2– and NH_3-TPD, and the results are shown in Fig. 7c and d. Clearly, the CO_2 desorption curves show two broad peaks, corresponding to the desorption of weakly and strongly adsorbed CO_2. Similarly, the NH_3 desorption curves show three peaks, associated with weak and medium/strong acid sites [52]. Table 2 summarizes the base/acid site distribution and density of the catalysts after the curves were deconvoluted. Interestingly, the variation in calcination temperature did not significantly affect the acidic and basic properties of the catalysts. This is likely because the basicity and acidity

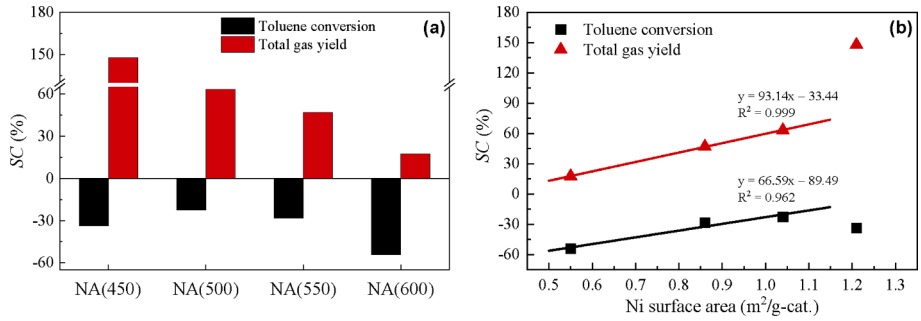

Fig. 8. Effect of calcination temperature of catalysts on the synergistic capacity calculated using toluene conversion and total gas yield (a), and correlation between the Ni surface area of catalyst and the synergistic capacity (b) (Reaction temperature: 450 °C; Packing material: quartz).

of the Ni/Al_2O_3 catalysts primarily arise from the alumina support [35,53]. As the γ-Al_2O_3 support used in this study was already calcined at 550 °C before use, calcining the precursor within the 450–600 °C range did not induce a notable or regular change in the basic and acidic properties of the catalysts. CO pulse chemisorption analysis was used to determine the Ni surface area, dispersion and particle size, and the results are presented in Table 3. The Ni surface area decreased with increasing calcination temperature, from 1.22 m^2/g-catal. of NA(450) to 0.55 m^2/g-catal. of NA(600). Notably, the lowest dispersion was obtained with NA(500) instead of NA(450). Despite this, increasing the calcination temperature appeared to enhance the metallic dispersion. On the other hand, the Ni particle sizes had an opposite trend to the dispersion with sizes ranging from 21.1 to 28.9 nm.

As previously mentioned, increasing the calcination temperature resulted in only minor variations in pore structure, base and acid properties, with a linear decrease in Ni surface area and nonlinear changes in dispersion and Ni particle size. In the catalyst-only case, the progressively decreasing conversion observed with increasing calcination temperature can be attributed to the decrease in Ni surface area, which leads to a reduction in available active sites, limiting toluene destruction. On the other hand, the change in total gas yield induced by the calcination temperature of the catalysts can be explained by Ni particle size (or dispersion), given the similar change trend. It is well-known that the size or dispersion of metal particles significantly influence catalyst selectivity and, therefore, the product distribution [54,55]. Additionally, in the plasma-catalytic process, the similar and decreasing trend in both conversion and total gas yield implies that the Ni surface area plays a crucial role in determining the reaction performance of plasma catalysis.

3.2.2. *Synergistic effect*

Fig. 8a shows the synergistic capacities calculated using toluene conversion and total gas yield for the different catalysts. No synergistic effect is observed in terms of toluene conversion. Catalysts calcined at higher temperatures tend to have lower synergistic capacities, except for NA(450). However, a clear synergistic effect is achieved in gas production regardless of the catalyst, with the synergistic capacity decreasing in the order of NA(450) > NA(500) > NA(550) > NA(600). The synergistic capacities for gas product selectivity and yield are presented in Fig. S9, showing that the synergistic effect in selectivity is mainly concentrated in NA(450), while for yield, a noticeable but weakening synergistic effect is observed at higher calcination temperatures. No synergistic effect is obtained for benzene and light hydrocarbons, except for CH_4.

As discussed earlier, the intensity of the synergistic effect appears to be closely related to the Ni surface area, which is supported by the negative correlation observed between the synergistic capacity in gas production and the calcination temperature of the catalysts. To investigate this relationship further, the correlation between Ni surface area and the synergistic capacity was analyzed for both toluene conversion

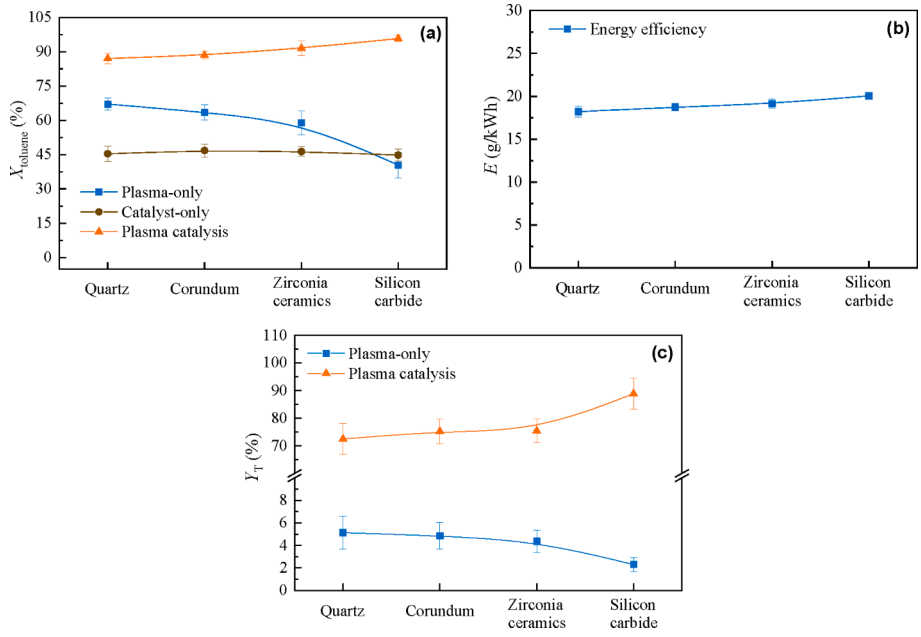

Fig. 9. Effect of packing material on toluene conversion (a), total gas yield (b) and energy efficiency (c) (Reaction temperature: 450 °C; Catalyst: NA(500)).

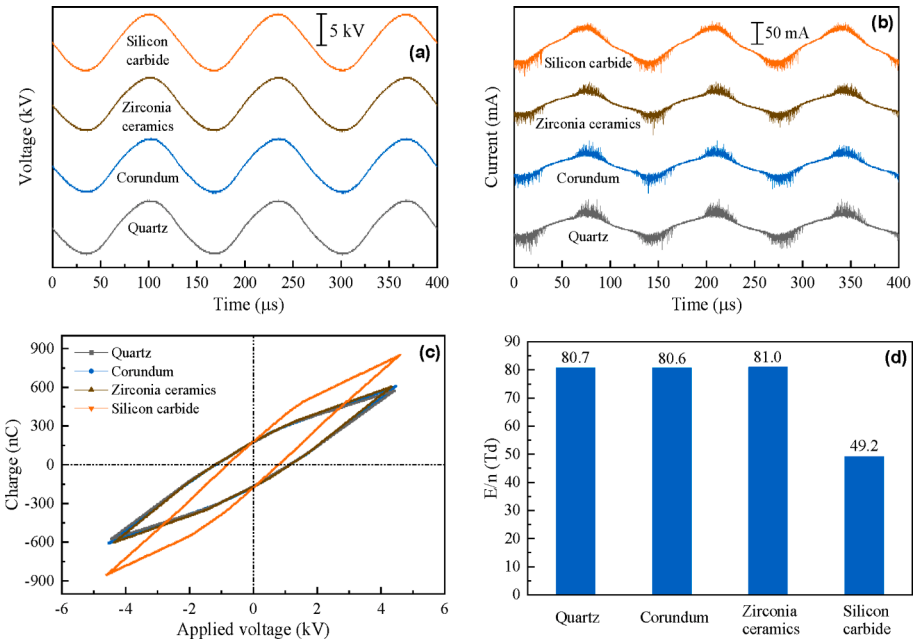

Fig. 10. Electrical signals of the DBD with different materials packing: Applied voltage signals (a), current signals (b), V-Q Lissajous curves (c) and E/n (d) (Reaction temperature: 450 °C; Catalyst: NA(500)).

and gas production, and the results are presented in Fig. 8b. Notably, the synergistic capacities obtained using NA(450) were not considered, as toluene was not detected at the outlet, making it difficult to estimate the actual values of toluene conversion and total gas yield. The results show a clear positive and linear correlation between Ni surface area and the synergistic capacity, suggesting that a higher Ni surface area is associated with a stronger synergistic effect. This finding can be explained by the fact that a higher Ni surface area provides more active sites, which increases the probability of generating a synergistic effect.

3.3. *Effect of relative permittivity of packing materials*

3.3.1. *Reaction performance*

The effect of the relative permittivity of packing materials was also investigated. Four packing materials were employed: quartz, corundum, zirconia ceramics, and silicon carbide, all of which were calcined at 950 °C for 6 h prior to use. Table S6 lists the composition and relative permittivity of these packing materials. The relative permittivity increases in the order of quartz < corundum < zirconia ceramics < silicon carbide, with silicon carbide having the highest relative permittivity of 200.3, which is much greater than that of the other materials.

The conversion obtained with different packing materials is presented in Fig. 9a. In catalyst-only experiments, the conversion remains at about 45% regardless of the packing material used, indicating that these materials have little thermal catalytic activity for toluene steam reforming. In the plasma-only mode, the use of high relative permittivity packing materials results in a decrease in conversion from about 67% with quartz packing to about 40% with silicon carbide packing. However, packing high relative permittivity materials in the plasma catalysis system leads to a slight increase in toluene conversion, and accordingly, the energy efficiency slightly increases from 18.2 g/kWh with quartz packing to 20.0 g/kWh with silicon carbide packing, as shown in Fig. 9b.

Taking into consideration the limited catalytic activity of the packing materials in the catalyst-only process, their effect on product generation is minimal and not considered significant. The impact of packing materials on the total gas yield is shown in Fig. 9c. In plasma-only experiments, the use of silicon carbide as the packing material results in the lowest total gas yield, while the other materials have similar values. However, under plasma catalysis, a noticeable difference in gas production is observed, particularly in the case of silicon carbide, which exhibits the highest total gas yield of about 90%, compared to the values of less than 80% obtained with other materials. Overall, the use of packing materials with high relative permittivity has both detrimental and promoting effects on the reaction performance of the plasma-only and plasma catalysis modes, respectively.

The effects of packing materials on the selectivity and yield of gas products and benzene in the plasma-only and plasma catalysis modes are illustrated in Figs. S14 and S15. In the plasma-only mode, there is only a slight variation in the selectivity and yield of gas products and benzene among quartz, corundum, and zirconia ceramics, while the use of silicon carbide leads to a significant decrease in the selectivity and yield of produced gases, along with a corresponding increase in benzene selectivity and yield. In the case of plasma catalysis, the differences in gas production among packing materials are more pronounced, particularly for silicon carbide, which results in higher CO and CH_4 selectivity, as well as higher H_2, CO, CO_2, and CH_4 yields, while also lowering the benzene selectivity and yield.

To further understand the effect of the relative permittivity of the packing materials, the discharge characteristics of the DBD packed with different materials are also characterized. Fig. 10 shows the electrical signals of the DBD packed with different materials and operated at a fixed discharge power. With the exception of silicon carbide, which shows the highest applied voltage of 9.2 kV_{pk-pk}, other materials have values of around 8.8 kV_{pk-pk}. As the relative permittivity of the packing materials used increases, the magnitude of current pulses gradually decreases, but the displacement current increases accordingly, especially in the case of silicon carbide. This phenomenon indicates that the use of packing materials with high relative permittivity could increase the component of surface discharge in DBD [42]. Higher relative permittivity materials are more effectively polarized, resulting in a stronger locally enhanced electric field, especially around the contact points between pellets [56]. Thus, surface discharge on the surface of pellets is easily ignited when using high relative permittivity packing material. Fig. 10c exhibits Lissajous curves of the DBD with different materials packing at a constant discharge power. Quartz, corundum, and zirconia ceramics have almost identical Lissajous curves, but that of silicon carbide is quite different. Table S4 summarizes discharge parameters calculated through different Lissajous curves, and the E/n is

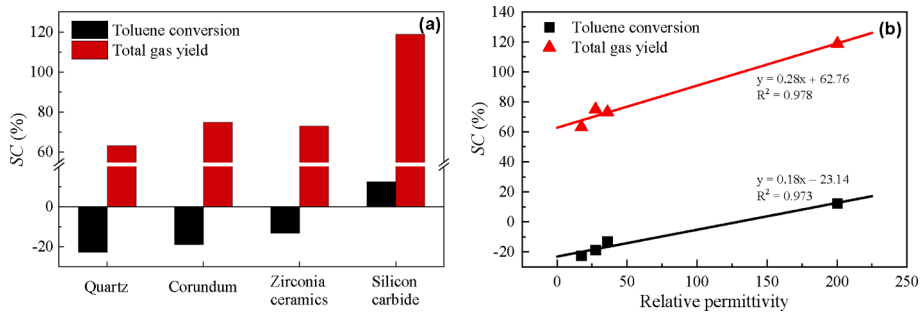

Fig. 11. Effect of packing material on the synergistic capacity calculated using toluene conversion and total gas yield (a), and correlation between the relative permittivity of packing material and the synergistic capacity (b) (Reaction temperature: 450 °C; Catalyst: NA(500)).

shown in Fig. 10d. Quartz, corundum, and zirconia ceramics have almost the same E/n values, which are much higher than that obtained with silicon carbide. Obviously, the three materials that possess close values of relative permittivity have close discharge parameters, but due to the large difference in relative permittivity, silicon carbide gets quite different values.

Based on the discharge characteristics results presented, it appears that in the plasma-only mode, the decrease in toluene conversion and total gas yield when using silicon carbide can be attributed to a decline in E/n. However, in the plasma catalysis mode, the results show that the use of silicon carbide leads to higher toluene conversion and total gas yield. This improvement is likely due to the increased surface discharge in the presence of silicon carbide.

3.3.2. *Synergistic effect*

Fig. 11a shows the synergistic capacities on conversion and total gas yield using different packing materials. The results indicate that all packing materials exhibit a synergistic effect in terms of gas production, with silicon carbide showing the highest synergistic capacity at around 120%, while the other materials have values around 70%. However, for toluene conversion, the synergistic effect is only observed in the case of silicon carbide, while the other materials show negative synergistic capacities around −15%.

We also investigated the effect of packing material on the synergistic capacities calculated based on the selectivity and yield of gas products, as shown in Fig. S10. The results indicate that the synergistic effect is observed in the selectivity of CO, as well as in the yield of H_2, CO, and CO_2. In particular, silicon carbide exhibits higher and lower synergistic capacities in the yield of main gas products and benzene, respectively, compared to other packing materials. Moreover, for light hydrocarbons the synergistic effect is mainly observed in the selectivity and yield of CH_4 and C_3 hydrocarbons.

We further examined the correlation between the relative permittivity of packing materials and the synergistic capacity in terms of toluene conversion and gas production, as shown in Fig. 11b. The results indicate that the synergistic capacity exhibits a positive and strong linear correlation with the relative permittivity of the packing materials. This finding suggests that the use of a packing material with high relative permittivity could enhance the synergistic effect.

The observed correlation may be attributed to the increased surface discharge in the case of packing materials with high relative permittivity. The greater surface discharge component implies that more area on the catalyst surface is covered by the discharge, as reported in previous studies [43]. Additionally, the active species generated by discharge and involved in surface reactions through Langmuir-Hinshelwood or Eley-Rideal mechanisms are considered key drivers of the synergistic effect [26]. However, most of the active species produced by discharge activation have a short lifetime [57]. Therefore, increasing the discharge-covered area on the catalyst surface could increase the probability of active species participating in surface reactions, thereby intensifying the synergistic effect.

In summary, the choice of packing material has a significant impact on the synergistic effect in plasma-catalytic processes, affecting the selectivity and yield of gas products. Moreover, using a packing material with high relative permittivity could lead to a stronger synergistic effect due to the increased surface discharge and higher probability of active species participating in surface reactions.

4. Conclusions

In this study, we investigated the performance of plasma-catalytic steam reforming of toluene in a DBD plasma reactor combined with Ni/γ-Al_2O_3 catalysts. The results showed that the toluene conversion and gas production were affected by the reaction temperature, catalyst calcination temperature, and packing material relative permittivity. At low reaction temperatures, the toluene conversion mainly depended on the intensity of the plasma, while gas production was limited. However, at high reaction temperatures, the increased catalyst activity promoted toluene conversion and enhanced the oxidation of carbonaceous species, leading to a greater production of gas products. The process achieved a high toluene conversion of 87.1%, a total gas yield of 72.6%, and an energy efficiency of 18.2 g/kWh at 450 °C. Furthermore, we found that the synergistic capacity of plasma catalysis was positively correlated with the metal surface area and relative permittivity of the packing materials, and negatively correlated with the reaction temperature in terms of toluene conversion. However, gas production had a positive correlation with reaction temperature. These findings suggest that using catalysts with lower calcination temperatures and packing materials with higher relative permittivity can improve the process efficiency. Overall, this work highlights the potential of plasma-catalytic steam reforming of toluene for sustainable hydrogen production and provides insights into optimizing the process parameters.

Declaration of Competing Interest

The authors declare that they have no known competing financial interests or personal relationships that could have appeared to influence the work reported in this paper.

Data availability

Data will be made available on request.

Acknowledgements

This work was financially supported by the National Natural Science Foundation of China (Grant No. 52106282), the National Key R&D Program of China (Grand No. 2019YFB1503902), the Strategic Priority Research Program of Chinese Academy of Sciences (Grand No. XDA21060600), the Science and Technology Program of Guangzhou (Grant No. 202102020292, 201904010098 and 202002030126) and the Natural Science Foundation of Guangdong Province of China (Grant No.

2019A1515011535). X. Tu thanks the support of the British Council Newton Fund Institutional Links Grant (No. 623389161). N. Wang thanks the University of Liverpool and the Chinese Scholarship Council for funding his PhD.

Appendix A. Supplementary data

Supplementary data to this article can be found online at https://doi.org/10.1016/j.cej.2023.142696.

References

[1] M. Antar, D. Lyu, M. Nazari, A. Shah, X. Zhou, D.L. Smith, Biomass for a sustainable bioeconomy: An overview of world biomass production and utilization, Renew. Sust. Energ. Rev. 139 (2021), 110691, https://doi.org/10.1016/j.rser.2020.110691.

[2] L. Cuiping, W. Chuangzhi, Yanyongjie, H. Haitao, Yanyongjie, H. Haitao, Chemical elemental characteristics of biomass fuels in China, Biomass Bioenerg. 27 (2004) 119–130, https://doi.org/10.1016/j.biombioe.2004.01.002.

[3] Ö. Tezer, N. Karabağ, A. Öngen, C.Ö. Çolpan, A. Ayol, Biomass gasification for sustainable energy production: A review, Int. J. Hydrogen Energ. 47 (2022) 15419–15433, https://doi.org/10.1016/j.ijhydene.2022.02.158.

[4] J. Han, H. Kim, The reduction and control technology of tar during biomass gasification/pyrolysis: An overview, Renew. Sust. Energ. Rev. 12 (2008) 397–416, https://doi.org/10.1016/j.rser.2006.07.015.

[5] C. Li, K. Suzuki, Tar property, analysis, reforming mechanism and model for biomass gasification-An overview, Renew. Sust. Energ. Rev. 13 (2009) 594–604, https://doi.org/10.1016/j.rser.2008.01.009.

[6] S. Anis, Z.A. Zainal, Tar reduction in biomass producer gas via mechanical, catalytic and thermal methods: A review, Renew. Sust. Energ. Rev. 15 (2011) 2355–2377, https://doi.org/10.1016/j.rser.2011.02.018.

[7] M.L. Valderrama Rios, A.M. González, E.E.S. Lora, O.A. Almazán del Olmo, Reduction of tar generated during biomass gasification: A review, Biomass Bioenerg. 108 (2018) 345–370, https://doi.org/10.1016/j.biombioe.2017.12.002.

[8] P. Hasler, T. Nussbaumer, Gas cleaning for IC engine applications from fixed bed biomass gasification, Biomass Bioenerg. 16 (1999) 385–395, https://doi.org/10.1016/S0961-9534(99)00018-5.

[9] Y. Chen, Y. Luo, W. Wu, Y. Su, Experimental investigation on tar formation and destruction in a lab-scale two-stage reactor, Energ. Fuel 23 (2009) 4659–4667, https://doi.org/10.1021/ef900623n.

[10] S. Kawi, J. Ashok, N. Dewangan, S. Pati, C. Junmei, Recent advances in catalyst technology for biomass tar model reforming: Thermal, plasma and membrane reactors, Waste Biomass Valori. 13 (2022) 1–30, https://doi.org/10.1007/s12649-021-01446-6.

[11] N. Gao, M.H. Milandile, C. Quan, L. Rundong, Critical assessment of plasma tar reforming during biomass gasification: A review on advancement in plasma technology, J. Hazard. Mater. 421 (2022), 126764, https://doi.org/10.1016/j.jhazmat.2021.126764.

[12] F. Saleem, J. Harris, K. Zhang, A. Harvey, Non-thermal plasma as a promising route for the removal of tar from the product gas of biomass gasification-A critical review, Chem. Eng. J. 382 (2020), 122761, https://doi.org/10.1016/j.cej.2019.122761.

[13] A.M. Harling, D.J. Glover, J.C. Whitehead, K. Zhang, Novel method for enhancing the destruction of environmental pollutants by the combination of multiple plasma discharges, Environ. Sci. Technol. 42 (2008) 4546–4550, https://doi.org/10.1021/es703213p.

[14] J. Ashok, S. Kawi, Low-temperature biomass tar model reforming over perovskite materials with DBD plasma: Role of surface oxygen mobility, Energ. Convers. Manage. 248 (2021), 114802, https://doi.org/10.1016/j.enconman.2021.114802.

[15] J. Yang, S. Liu, T. He, L. Nengzi, Y. Wang, L. Su, J. Cao, L. Ji, C. Yuan, M. Geng, Degradation of toluene by DBD plasma-catalytic method with $Mn_xCo_yCe_zO_n$ catalysts: Characterization of catalyst, catalytic activity and continuous test, J. Environ. Chem. Eng. 9 (2021), 106361, https://doi.org/10.1016/j.jece.2021.106361.

[16] F. Saleem, A. Abbas, A. Rehman, A.H. Khoja, S.R. Naqvi, M.Y. Arshad, K. Zhang, A. Harvey, Decomposition of benzene as a biomass gasification tar in CH_4 carrier gas using non-thermal plasma: Parametric and kinetic study, J. Energy. Inst. 102 (2022) 190–195, https://doi.org/10.1016/j.joei.2022.03.009.

[17] K. Xiao, X. Li, J. Santoso, H. Wang, K. Zhang, J. Wu, D. Zhang, Synergistic effect of dielectric barrier discharge plasma and Mn catalyst on CO_2 reforming of toluene, Fuel 285 (2021), 119057, https://doi.org/10.1016/j.fuel.2020.119057.

[18] S.A. Nair, A.J.M. Pemen, K. Yan, F.M. van Gompel, H.E.M. van Leuken, E.J.M. van Heesch, K.J. Ptasinski, A.A.H. Drinkenburg, Tar removal from biomass-derived fuel gas by pulsed corona discharges, Fuel Process. Technol. 84 (2003) 161–173, https://doi.org/10.1016/s0378-3820(03)00053-5.

[19] A.J.M. Pemen, S.A. Nair, K. Yan, E.J.M. van Heesch, K.J. Ptasinski, A.A.H. Drinkenburg, Pulsed corona discharges for tar removal from biomass derived fuel gas, Plasmas Polym. 8 (2003) 209–224, https://doi.org/10.1023/a:1024813306111.

[20] R. Xu, X. Kong, H. Zhang, P.M. Ruya, X. Li, Destruction of gasification tar over Ni catalysts in a modified rotating gliding arc plasma reactor: Effect of catalyst position and nickel loading, Fuel 289 (2021), 119742, https://doi.org/10.1016/j.fuel.2020.119742.

[21] D. Mei, P. Zhang, S. Liu, L. Ding, Y. Ma, R. Zhou, H. Gu, Z. Fang, P.J. Cullen, X. Tu, Highly efficient reforming of toluene to syngas in a gliding arc plasma reactor, J. Energy. Inst. 98 (2021) 131–143, https://doi.org/10.1016/j.joei.2021.06.005.

[22] X. Kong, A. Wu, S. Fu, R. Xu, Y. Zhao, X. Li, J. Yan, Comparatively investigation of real MSW and biomass tar treatment by a rotating gliding arc, Fuel 298 (2021), 120745, https://doi.org/10.1016/j.fuel.2021.120745.

[23] M. Wnukowski, P. Jamróz, L. Niedzwiecki, The role of hydrogen in microwave plasma valorization of producer gas, Int. J. Hydrogen Energ. 48 (2021) 11640–11651, https://doi.org/10.1016/j.ijhydene.2021.05.031.

[24] J. Li, J. Tao, B. Yan, K. Cheng, G. Chen, J. Hu, Microwave reforming with char-supported Nickel-Cerium catalysts: A potential approach for thorough conversion of biomass tar model compound, Appl. Energ. 261 (2020), 114375, https://doi.org/10.1016/j.apenergy.2019.114375.

[25] J.V. Durme, J. Dewulf, C. Leys, H.V. Langenhove, Combining non-thermal plasma with heterogeneous catalysis in waste gas treatment: A review, Appl. Catal. B Environ. 78 (2008) 324–333, https://doi.org/10.1016/j.apcatb.2007.09.035.

[26] E. Neyts, A. Bogaerts, Understanding plasma catalysis through modelling and simulation-A review, J. Phys. D Appl. Phys. 47 (2014), 224010, https://doi.org/10.1088/0022-3727/47/22/224010.

[27] K. Tao, N. Ohta, G. Liu, Y. Yoneyama, T. Wang, N. Tsubaki, Plasma enhanced catalytic reforming of biomass tar model compound to syngas, Fuel 104 (2013) 53–57, https://doi.org/10.1016/j.fuel.2010.05.044.

[28] B. Xu, N. Wang, J. Xie, Y. Song, Y. Huang, W. Yang, X. Yin, C. Wu, Removal of toluene as a biomass tar surrogate by combining catalysis with nonthermal plasma: Understanding the processing stability of plasma catalysis, Catal. Sci. Technol. 10 (2020) 6953–6969, https://doi.org/10.1039/D0CY01211D.

[29] L. Liu, Q. Wang, J. Song, S. Ahmad, X. Yang, Y. Sun, Plasma-assisted catalytic reforming of toluene to hydrogen rich syngas, Catal. Sci. Technol. 7 (2017) 4216–4231, https://doi.org/10.1039/c7cy00970d.

[30] L. Liu, Q. Wang, S. Ahmad, X. Yang, M. Ji, Y. Sun, Steam reforming of toluene as model biomass tar to H_2-rich syngas in a DBD plasma-catalytic system, J. Energy. Inst. 91 (2018) 927–939, https://doi.org/10.1016/j.joei.2017.09.003.

[31] L. Liu, J. Dai, S. Das, Y. Wang, H. Yu, S. Xi, Z. Zhang, X. Tu, Plasma-catalytic CO_2 reforming of toluene over hydrotalcite-derived NiFe/(Mg, Al)O_x catalysts, JACS Au 3 (2023) 785–800, https://doi.org/10.1021/jacsau.2c00603.

[32] D. Mei, S. Liu, Y. Wang, H. Yang, Z. Bo, X. Tu, Enhanced reforming of mixed biomass tar model compounds using a hybrid gliding arc plasma catalytic process, Catal. Today 337 (2019) 225–233, https://doi.org/10.1016/j.cattod.2019.05.046.

[33] B. Xu, J. Xie, H. Zhan, X. Yin, C. Wu, H. Liu, Removal of toluene as a biomass tar surrogate in a catalytic nonthermal plasma process, Energ. Fuel 32 (2018) 10709–10719, https://doi.org/10.1021/acs.energyfuels.8b02444.

[34] G. Guan, M. Kaewpanha, X. Hao, A. Abudula, Catalytic steam reforming of biomass tar: Prospects and challenges, Renew. Sust. Energ. Rev. 58 (2016) 450–461, https://doi.org/10.1016/j.rser.2015.12.316.

[35] H. Özdemir, M.A.F. Öksüzömer, M.A. Gürkaynak, Effect of the calcination temperature on Ni/$MgAl_2O_4$ catalyst structure and catalytic properties for partial oxidation of methane, Fuel 116 (2014) 63–70, https://doi.org/10.1016/j.fuel.2013.07.095.

[36] S. Velu, S.K. Gangwal, Synthesis of alumina supported nickel nanoparticle catalysts and evaluation of nickel metal dispersions by temperature programmed desorption, Solid State Ionics 177 (2006) 803–811, https://doi.org/10.1016/j.ssi.2006.01.031.

[37] M. Kong, Q. Yang, J. Fei, X. Zheng, Experimental study of Ni/MgO catalyst in carbon dioxide reforming of toluene, a model compound of tar from biomass gasification, Int. J. Hydrogen Energ. 37 (2012) 13355–13364, https://doi.org/10.1016/j.ijhydene.2012.06.108.

[38] F. Zhu, H. Zhang, H. Yang, J. Yan, X. Li, X. Tu, Plasma reforming of tar model compound in a rotating gliding arc reactor: Understanding the effects of CO_2 and H_2O addition, Fuel 259 (2020), 116271, https://doi.org/10.1016/j.fuel.2019.116271.

[39] D. Mei, Y. Wang, S. Liu, M. Alliati, H. Yang, X. Tu, Plasma reforming of biomass gasification tars using mixed naphthalene and toluene as model compounds, Energ. Convers. Manage. 195 (2019) 409–419, https://doi.org/10.1016/j.enconman.2019.05.002.

[40] W. Wang, Y. Ma, G. Chen, C. Quan, J. Yanik, N. Gao, X. Tu, Enhanced hydrogen production using a tandem biomass pyrolysis and plasma reforming process, Fuel Process. Technol. 234 (2022), 107333, https://doi.org/10.1016/j.fuproc.2022.107333.

[41] Y. Wang, Y. Chen, J. Harding, H. He, A. Bogaerts, X. Tu, Catalyst-free single-step plasma reforming of CH_4 and CO_2 to higher value oxygenates under ambient conditions, Chem. Eng. J. 450 (2022), 137860, https://doi.org/10.1016/j.cej.2022.137860.

[42] X. Tu, H.J. Gallon, M.V. Twigg, P.A. Gorry, J.C. Whitehead, Dry reforming of methane over a Ni/Al_2O_3 catalyst in a coaxial dielectric barrier discharge reactor, J. Phys. D Appl. Phys. 44 (2011), 274007, https://doi.org/10.1088/0022-3727/44/27/274007.

[43] X. Tu, H.J. Gallon, J.C. Whitehead, Transition behavior of packed-bed dielectric barrier discharge in argon, IEEE Trans. Plasma Sci. 39 (2011) 2172–2173, https://doi.org/10.1109/TPS.2011.2160289.

[44] S. Xu, P.I. Khalaf, P.A. Martin, J.C. Whitehead, CO_2 dissociation in a packed-bed plasma reactor: effects of operating conditions, Plasma Sources Sci. Technol. 27 (2018), 075009, https://doi.org/10.1088/1361-6595/aacd6a.

[45] G.J.M. Hagelaar, L.C. Pitchford, Solving the Boltzmann equation to obtain electron transport coefficients and rate coefficients for fluid models, Plasma Sources Sci. Technol. 14 (2005) 722–733, https://doi.org/10.1088/0963-0252/14/4/011.
[46] Y. Itikawa, N. Mason, Cross sections for electron collisions with water molecules, J. Phys. Chem. Ref. Data 34 (2005) 1–22, https://doi.org/10.1063/1.1799251.
[47] Y. Itikawa, Cross sections for electron collisions with nitrogen molecules, J. Phys. Chem. Ref. Data 35 (2006) 31–53, https://doi.org/10.1063/1.1937426.
[48] M. Sugasawa, T. Terasawa, S. Futamura, Additive effect of water on the decomposition of VOCs in nonthermal plasma, IEEE Trans. Ind. Appl. 46 (2010) 1692–1698, https://doi.org/10.1109/TIA.2010.2057390.
[49] S. Liu, D. Mei, L. Wang, X. Tu, Steam reforming of toluene as biomass tar model compound in a gliding arc discharge reactor, Chem. Eng. J. 307 (2017) 793–802, https://doi.org/10.1016/j.cej.2016.08.005.
[50] L. Yu, X. Li, X. Tu, Y. Wang, S. Lu, J. Yan, Decomposition of naphthalene by DC gliding arc gas discharge, J. Phys. Chem. A 114 (2010) 360–368, https://doi.org/10.1021/jp905082s.
[51] J. Zhang, H. Xu, X. Jin, Q. Ge, W. Li, Characterizations and activities of the nano-sized Ni/Al_2O_3 and $Ni/La\text{-}Al_2O_3$ catalysts for NH_3 decomposition, Appl. Catal. A Gen. 290 (2005) 87–96, https://doi.org/10.1016/j.apcata.2005.05.020.
[52] N.D. Charisiou, G. Siakavelas, K.N. Papageridis, A. Baklavaridis, L. Tzounis, K. Polychronopoulou, M.A. Goula, Hydrogen production via the glycerol steam reforming reaction over nickel supported on alumina and lanthana-alumina catalysts, Int. J. Hydrogen Energ. 42 (2017) 13039–13060, https://doi.org/10.1016/j.ijhydene.2017.04.048.
[53] L. Smoláková, M. Kout, E. Koudelková, L. Čapek, Effect of calcination temperature on the structure and catalytic performance of the Ni/Al_2O_3 and $Ni\text{-}Ce/Al_2O_3$ catalysts in oxidative dehydrogenation of ethane, Ind. Eng. Chem. Res. 54 (2015) 12730–12740, https://doi.org/10.1021/acs.iecr.5b03425.
[54] R. Cuevas-García, J.G. Téllez-Romero, J. Ramírez, P. Sarabia-Bañuelos, I. Puente-Lee, C. Salcedo-Luna, S. Hernández-González, V.A. Nolasco-Arizmendi, Effect of the preparation method on particle size and reaction selectivity on naphthalene hydrogenation over Ni/H-MOR catalysts, Catal. Today 360 (2021) 63–71, https://doi.org/10.1016/j.cattod.2019.08.044.
[55] H.C. Wu, Y.C. Chang, J.H. Wu, J.H. Lin, I.K. Lin, C.S. Chen, Methanation of CO_2 and reverse water gas shift reactions on Ni/SiO_2 catalysts: The influence of particle size on selectivity and reaction pathway, Catal. Sci. Technol. 5 (2015) 4154–4163, https://doi.org/10.1039/C5CY00667H.
[56] Y. Zhang, H. Wang, W. Jiang, A. Bogaerts, Two-dimensional particle-in cell/Monte Carlo simulations of a packed-bed dielectric barrier discharge in air at atmospheric pressure, New J. Phys. 17 (2015), 083056, https://doi.org/10.1088/1367-2630/17/8/083056.
[57] V.A. Bityurin, E.A. Filimonova, G.V. Naidis, Simulation of naphthalene conversion in biogas initiated by pulsed corona discharges, IEEE Trans. Plasma Sci. 37 (2009) 911–919, https://doi.org/10.1109/TPS.2009.2019756.